CHAPTER THREE

THEORY OF PRECIPITATION REACTIONS IN STEELS

3.1 INTRODUCTION

The formation and subsequent behaviour of individual particles in any precipitation process involve its nucleation, growth and coarsening but the overall precipitation process must account for solute concentration impingement effects. In some cases the nucleation of second phases in steel might involve the dissolution of metastable precipitates and the coarsening of stable precipitates. These stages of nucleation and growth of the precipitates will be discussed in this chapter.

3.2 CLASSICAL THEORY OF NUCLEATION

Most particle-sized second phases in steels precipitate through a nucleation and growth mechanism. During the nucleation process, the associated free energy change is dominated by the Gibbs chemical free energy, the surface free energy and the misfit free energy terms. The total free energy change can be represented by summing all of these contributions:

$$\Delta G = \frac{4}{3}\pi r^3 \Delta G_v + 4\pi r^2 \gamma + \frac{4}{3}\pi r^3 \Delta G_\varepsilon \text{, (where } \Delta Gv \leq 0) \qquad \text{Equation 3.1}$$

where ΔG_v is the Gibbs chemical free energy released per unit volume of the new phase and has a negative value, γ is the interfacial surface energy per unit area associated with the interface of the two phases and ΔG_ε is the misfit strain energy per unit volume. Plotting this equation demonstrates the dependency of the stability of the new embryo on its size, see Figure 3.1.

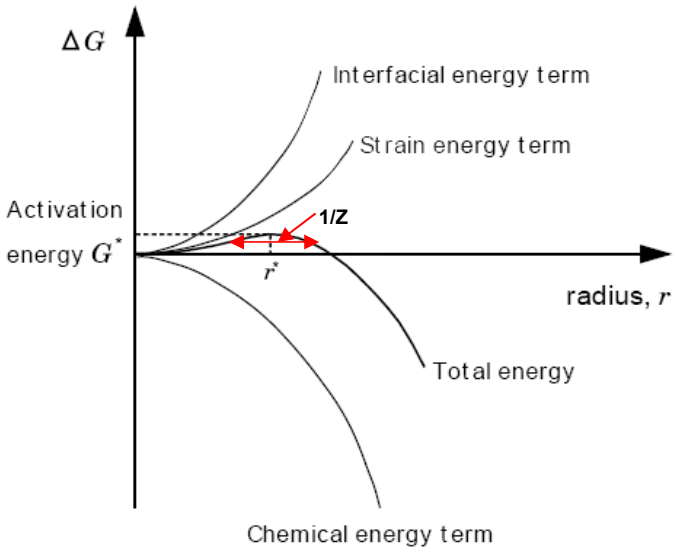

Figure 3.1 The free energy change associated with the formation of a stable nucleus with the radius r.

3.2.1 Activation Energy for Nucleation within the Matrix

From Figure 3.1, the maximum total free energy occurs at a critical radius r^* when the free energy has a value ΔG^*, known as the activation energy. An embryo with a radius larger than r^* will tend to grow spontaneously rather than dissolve since its growth leads to a decrease in free energy and then the embryo becomes a stable nucleus. At

$r = r^*$, $d\Delta G/dr$ equals zero, so that ΔG^* is given by:

$$r^* = \frac{-2\gamma^2}{(\Delta G_v + \Delta G_\varepsilon)} \qquad \text{Equation 3.2}$$

$$\Delta G^* = \frac{16\pi\gamma^3}{3(\Delta G_v + \Delta G_\varepsilon)^2} \qquad \text{Equation 3.3}$$

3.2.2 Activation Energy for Nucleation on the Grain Boundary

In the preceding section, the formation of a nucleus has been regarded as a homogeneous process occurring with equal probability in all parts of the assembly. In practice, this is unlikely to happen unless the assembly is extremely pure, and also contains (if in the solid state) very few structural defects. More usually, the presence of impurity particles and structural defects (dislocations and sub- and grain boundaries)

that enable nuclei to be formed with a much smaller free energy of activation than that of the homogeneous nuclei, occurs in most industrial alloys.

If we consider nucleation that takes place on a grain boundary, a certain surface area A of the grain boundary is removed from the system. This forms an additional driving force for nucleation and must, therefore, have a negative sign in the basic free energy equation for nucleation (see the last term in Equation 3.4 below).

$$\Delta G = K_1\{\Delta G_v + \Delta G_\varepsilon\} + K_2\gamma_{ppt}A_{ppt} + K_3\gamma_{ppt/gb}A_{ppt/gb} - \gamma_{gb}A_{gb} \qquad \text{Equation 3.4}$$

From this equation it is clear that the system will preferentially select those higher energy grain boundary sites first where it will gain the most energy as an additional driving force.

The following relationship between the activation energy for grain boundary nucleation for the various possible grain boundary sites and the contact angle θ should, therefore, be expected, Figure 3.2. The ratio of the free energy required to form a grain boundary nucleus to that needed to form a homogeneous nucleus obviously decreases as the ratio of the grain boundary energy to the interphase boundary energy increases through the contact angle parameter cos θ.

From Figure 3.2 it may be seen that at a given contact angle θ, nucleation on grain corners requires the lowest activation energy, then grain edges and lastly grain boundaries. Grain boundaries can also lower the retarding force arising from the strain energy ΔG_ε and, thereby, create a new driving force. In cases where the surface energy and the strain energy are lowered enough through nucleation on grain boundaries, the grain boundaries may become the preferred sites fully and no nucleation within the grains will occur. This is what is typically found in Al - Mg alloys where the β-phase nucleates only on grain boundaries and embrittles the alloy [95].

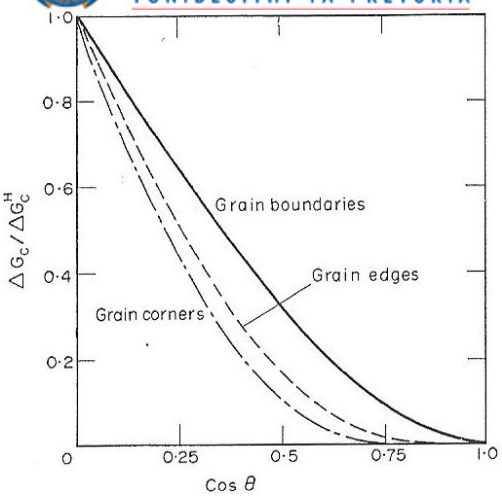

Figure 3.2. The ratio of the free energy required to form a nucleus on various types of grain boundary sites to that required to form a nucleus in the grain matrix, is plotted as a function of the contact angle parameter *cos* θ.

Precipitates on grain boundaries represent a special case because they are located on the junction of two or more different crystal orientations and may also possess different interface lattice parameters in the case of interphase boundaries. Figure 3.3 shows different possibilities of interfaces on a boundary.

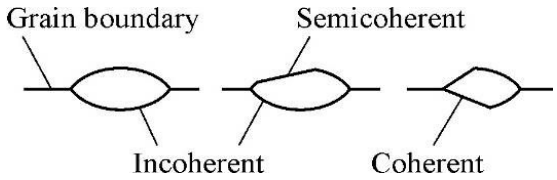

Figure 3.3. Different possibilities of the precipitate's interface on grain boundaries.

3.2.3 MISFIT STRAIN ENERGY AROUND THE PARTICLE

The structural misfit across a matrix / precipitate interface plays a prominent role in the strain energy around a coherent or semi coherent precipitate. This misfit very often leads to interfacial dislocations or ledges and steps. For incoherent particles the strain energy arises mainly out of the differences in the lattice spacing and the strain in the matrix volume because of differences in densities. Nabarro [96] derived the elastic strain energy for an ellipsoidal nucleus of β phase having semi-axes *a, a and c* in an isotropic α matrix as [108]:

$$\Delta G_{\varepsilon} = \frac{2}{3} G_m \delta^2 \nu^{\beta} f(c/a) \qquad \text{Equation 3.5}$$

where G_m is the shear modulus of the matrix, δ is the volume misfit of the precipitate in the matrix and is defined as:

$$\delta = \frac{\nu^{\beta} - \nu^{\alpha}}{\nu^{\beta}} = \qquad \text{Equation 3.6}$$

where ν^{β} and ν^{α} are the lattice spacings of the precipitate phase and the matrix, respectively. Thus the elastic strain energy is proportional to the square of the volume misfit, δ^2. The function $f(c/a)$ is a factor that takes into account the shape effect and is shown in Figure 3.4.

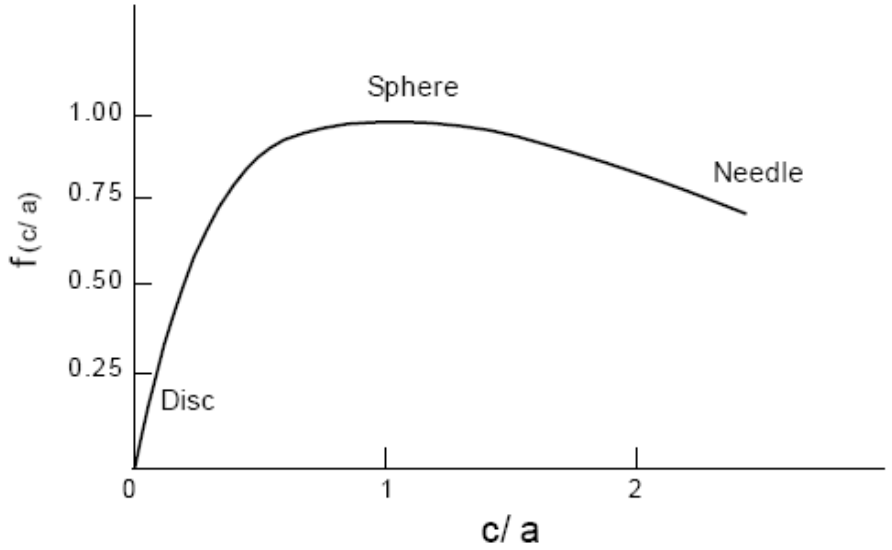

Figure 3.4. Illustration of the variation of the function f(c/a) of an incoherent nucleus with its shape.

A flat disc, therefore, provides a lower value of ΔG_{ε} but also has a higher surface area per unit volume and this results in a higher total surface energy. Therefore, a compromise has to be reached which very often leads to ellipsoidal shapes.

3.2.4 INTERFACIAL ENERGY

Boundaries between different solid phases can be classified into coherent, semi-coherent and incoherent interfaces. For nucleation in crystalline solids the interfacial energy γ can vary widely from very low values for a coherent interface to high values for an incoherent interface. The interfacial energy is a vital parameter for kinetic simulations. Even small variations of this parameter can have a massive impact on the nucleation and also strongly influences growth and coarsening of precipitates. The

value of this energy is not often known, since it depends on the crystallography of the precipitate and matrix, on the chemical composition of involved phases, on their misorientation, the degree of coherency and finally, any segregation effects of other minor elements to the interface. Commonly, a mean value of the interfacial energy is used in numeric simulations, which is denoted as an "effective interfacial energy" γ. It is of great importance, therefore, to evaluate possibilities to predict these parameters from existing data (e.g. thermodynamic databases). To treat the problem of multi-component, multi-phase, multi-particle precipitation kinetics on a more physical basis it is necessary to predict the interfacial energies of the precipitates depending on the actual system state.

3.2.4.1 FULLY COHERENT PRECIPITATES

A coherent interface arises when all the lattice planes of the two phases are continuous across the interface. An interface is said to be fully coherent if each atomic plane in one crystal that intersects the interface, is matched by another plane on the opposite side of the interface.

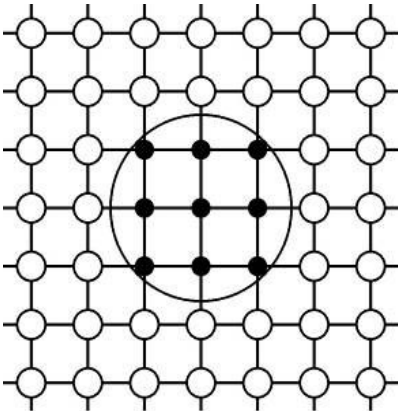

Figure 3.5. Fully coherent precipitates, with no broken inter-atom bonds and with δ=0. The interface is indicated by the circle.

The interface energy in the case of the two lattice spacings with no difference ($\delta = 0$) is only of a chemical nature through the bond-energy of atoms A and B, because there is no structural difference between their lattice spacings. Fully coherent precipitates occur whenever there is no or only insignificant lattice mismatch, at least in one direction.

Especially small precipitates often meet this condition; for example *Guinier-Preston*[1] (GP) zones in many Al-alloys. If there is no lattice mismatch at all these interfaces show identical, usually very low, interfacial energy values in every direction (see Figure 3.5). Consequently, these precipitates are usually spheres, for example in the Al-4at% Ag model alloy [97].

If the lattice parameters of the precipitate and matrix differ, considerable strain energy can be the result. Because of the different lattice structures of precipitate and matrix, the lattice will be deformed elastically, depending on the Young's modulus and also depending on the orientation of the particle in the lattice. For example, a situation where a particle has a similar lattice parameter in a horizontal direction but not in a vertical direction, is illustrated in Figure 3.6. To keep the misfit energy to a minimum these precipitates arrange themselves in the horizontal direction and develop plate or needle like shapes. Similar misfits in every direction will also lead to a spherical particle.

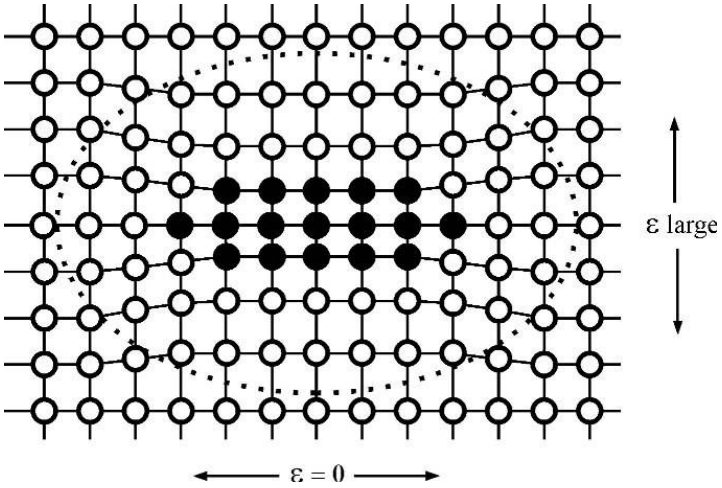

Figure 3.6. Coherent precipitate with different lattice parameters only in the vertical direction. The volume influenced by the lattice misfit, ε is marked by the dotted line.

3.2.4.2 INCOHERENT PRECIPITATES

When the interfacial plane has a very different atomic configuration in the two adjoining planes, or even if it is similar but the inter-atomic distances of the two phases differ by more than 25 %, there will not be good matching across the interface and the interface will most probably be incoherent [98]. During the evolution of a precipitate, it is very

[1] e.g.: Al-Cu system with monatomic, disc shaped, Cu layer in (100) plain. Fully coherent with matrix, typical diameter of 3-10nm

likely that the effective interfacial energy changes depending on the actual size and composition of the particle. A small precipitate when the ΣA/ΣV of the second phase is still large, will probably start with fully coherent interfaces and introduce only low elastic strains, despite a possible lattice misfit. During growth as the ΣA/ΣV decreases, some interfaces can transform themselves into semi coherent interfaces to reduce the elastic strain energy. This coherency loss is accompanied by the formation of vacancies and/or misfit dislocations in the interface.

3.2.4.3 SEMI-COHERENT PRECIPITATES

Semi coherent precipitates share some coherent and some incoherent interfaces with the matrix, depending on the crystal orientation. The strain associated with a coherent interface raises the total free energy of the system, and for a sufficiently large atomic misfit, it would be energetically more favourable to replace the coherent interface with a semi-coherent interface in which the misfit is periodically taken up by misfit dislocations.

Summarising these findings, the interfacial energy is dependent on crystallographic and chemical parameters and is not a single scalar value in general. For practical reasons an effective interfacial energy is often introduced in computer simulations.

3.2.5 NUCLEATION RATE

The probability of the barrier to nucleation being overcome by a potential nucleus is given by a Boltzman expression, and so the concentration of critical – sized nuclei N^*:

$$N^* = N_0 \exp\left(\frac{-\Delta G^*}{kT}\right) \qquad \text{Equation 3.7}$$

where N_0 is the initial number density of nucleation sites per unit volume, and k is the Boltzman constant. Each critical sized embryo can be made supercritical and become a nucleus by transferring an atom in contact with the embryo into it.

In the absence of the soft impingement, whereby the mean solute concentration decreases as the reaction proceeds, the nucleation rate is assumed to occur at a constant rate, and this is difficult to justify experimentally because of the different precipitation reactions that occur simultaneously [5,99,100,101,103,104]. Classical nucleation theory is used to estimate the nucleation rate for each type of precipitate. There are several formulae for the nucleation rate per unit volume that are based on the

Turnbull and Fisher nucleation model [95]. Following this model the nucleation rate can be written as:

$$\dot{N} = \left(1 - \frac{V'}{V^{eq}}\right) N_o \frac{kT}{h} \exp\left(-\frac{\Delta G^* + Q}{RT}\right) \qquad \text{Equation 3.8}$$

where Q is the activation energy for diffusion, k and h are the Boltzmann and Planck constants respectively, T is the absolute temperature, V' and V^{eq} are instantaneous and equilibrium volume fractions of alloy precipitates, respectively. The term $(1 - V'/V^{eq})$ is commonly used in the Avrami theory to account for the matrix which can no longer contribute to the transformation and that has been incorporated in the equation to account for the fact that nucleation sites are consumed as transformation proceeds [104].

If long-range diffusion occurs as in carbide precipitation, the expression $\exp(-Q/RT)$ will be multiplied by the mole fraction $\bar{c}$ of the slowest moving solute (in this case niobium) [5,104,100]. Then the nucleation rate per unit volume in this instance is given by:

$$\dot{N} = \bar{c}\left(1 - \frac{V'}{V^{eq}}\right) N_o \frac{kT}{h} \exp\left(-\frac{\Delta G^* + Q}{RT}\right) \qquad \text{Equation 3.9}$$

The calculation of ΔG^* requires a knowledge of the chemical driving force for nucleation ΔG_v, which depends on the chemical composition of the alloy and the equilibrium concentrations (which determine the initial supersaturation) or alternatively, by the undercooling ΔT below the equilibrium transformation temperature. There are two unknowns that cannot be determined experimentally for a complete reaction kinetic calculation of precipitates to be made, that is, the interfacial energy (γ) and the initial number of nucleation site (N_0). These parameters are treated as fitting parameters and the sensitivity of the results in the context of M_6C carbide precipitation in Fe–C–Nb steel, has been made previously by Fujita et al. [103]. Their results show that the nucleation rate is affected more by the interfacial energy than by the number density.

3.2.6 The Time-Dependent Nucleation Rate

The above equilibrium model did not include the likelihood of the particle's size greater than the critical embryo, r^* ever decaying. According to the *Becker-Döring* theory a decay of nuclei with $r > r^*$ is still likely. This is accounted for by the *Zeldovich* factor Z.

A nucleus is supercritical when the size is larger than the size range indicated by 1/Z in Figure 3.1.

According to the classical theory of nucleation, a general time-dependent equation for calculating the rate of isothermal nucleation is given by:

$$\dot{N} = Z\beta^* N_o \exp\left(-\frac{\Delta G^*}{kT}\right)\exp\left(\frac{\tau}{t}\right) \qquad \text{Equation 3.10}$$

where β^* is the atomic impingement rate (which includes the temperature dependent diffusion rate), N_o the number of available nucleation sites. The simulation time is t, k is the Boltzmann constant, T is the absolute temperature, and τ is the incubation time. The gradient of the driving force ΔG within the region $1/Z$ is rather small and the cluster will move across this region predominantly by random walk with the jump frequency β^*. The expected time to cover the distance $1/Z$ is identified with the incubation time τ:

$$\tau = \frac{1}{2\beta^* Z^2} \qquad \text{Equation 3.11}$$

$$\beta^* = \frac{4\pi r^{*2} D c_\alpha}{a^4} \qquad \text{Equation 3.12}$$

where a is the mean atomic lattice distance of the matrix phase, D is the diffusion coefficient of the rate controlling solute atoms in the matrix and c_α is the equilibrium solute composition within the matrix. The atomic impingement rate β^* is the effective rate, or probability, with which the atoms change from the matrix to the nucleus surface and is, therefore, temperature dependent. Equation 3.12 holds true for spherical nuclei and a binary system.

3.2.7 Chemical Driving Force

One of the critical parameters that are needed for the calculation, that is, ΔG_V the chemical free energy change per unit volume of precipitate, is given by:

$$\Delta G_V = \frac{\Delta G}{\upsilon^i V^{i\alpha}} \qquad \text{Equation 3.13}$$

where υ is the molar volume of the i^{th} phase and ΔG is the molar free energy change of the precipitate reaction, $V^{i\alpha}$ is the maximum volume fraction of the i^{th} phase. ΔG

for the formation of some of the niobium carbides can be obtained with a CALPHAD method via explicit equations (see Section 2.11, Equations 2.16 – 2.20, which are based on minimising the Gibbs free energy relative to the standard element reference state) [102,103,104,105].

In multi-component systems of the type Fe-C-Nb-Ti, there are thermodynamic data available for the carbides and nitrides, but unfortunately not for the Laves phase (Fe_2Nb) and M_6C (Fe_3Nb_3C) type carbides. However, recently the solubility products for these phases that can be used to estimate ΔG have been determined [6,106]. Table 1 below shows the solubility products of the precipitates within the ferrite matrix.

Table 4. Solubility products of the precipitates within a ferrite matrix.

System	Product	Soluble phase
TiN	–	Ferrite
TiC	log[Ti][C] = 4.4 – 9575/T	Ferrite
NbN	log[Nb][N] = 4.96 – 12230/T	Ferrite
NbC	log[Nb][C] = 5.43 – 10960/T	Ferrite
Fe_3Nb_3C	$\log[Nb]^3[C] = 5.2178 - 11613/T$	Ferrite*
Fe_2Nb	log[Nb] = 2.4646 – 3780.3/T	Ferrite*

*These solubility products were determined by Fujita and co-workers [6]

Fujita et al [6] have attempted to find thermodynamic parameters using the solubility products, and these expressions with the mole fractions (e.g. $x_{Nb}^{\alpha\beta}$) for the free energy changes of the precipitation reactions from a niobium – supersaturated ferrite matrix, are given by:

Fe_3Nb_3C (β); $\Delta G^{\beta} = -222509 - RT\{6.423 + \ln(x_{Nb}^{\alpha\beta})^3(x_C^{\alpha\beta})\}$

Fe_2Nb (γ); $\Delta G^{\gamma} = -72334 - RT\{0.5469 + \ln x_{Nb}^{\alpha\gamma}\}$

3.3 GROWTH BY SUPERSATURATION

Attempts to model particle growth by a decrease in supersaturation in a ternary or a higher system have been made by assuming a binary approach in which only solutes are considered in the growth equations; thereby violating local equilibrium at the interface. Bhadeshia stated that the procedure for modelling particle growth is falsely justified by stating that the solute considered is the one that controls growth, despite the fact that the theory of diffusion in multi-component systems has been well established [105].

3.3.1 DIFFUSION CONTROLLED GROWTH RATE

A reasonable approximation for isothermal diffusion controlled growth in a binary alloy is that the compositions of the phases in contact at the interface are locally in equilibrium. It follows that the concentrations are given by a tie–line on the equilibrium phase diagram. For a binary system, the tie–line is unique and passes through $\bar{c}$, which is the average concentration of the solute in the matrix alone. The concentration profile that develops during the precipitation of a solute–rich phase such as carbides, is shown in Figure 3.7, where $c^{\alpha\beta}$ is the concentration of the solute in the ferrite (α) matrix which is in equilibrium with the precipitate (β) and $c^{\beta\alpha}$ is the corresponding concentration in the β which is in equilibrium with α; whereas both are obtained from the phase diagram.

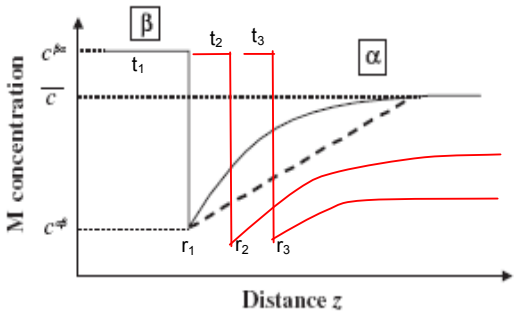

Figure 3.7. The solute concentration profile during diffusion - controlled growth of β from α. $c^{\alpha\beta}$ and $c^{\beta\alpha}$ are concentrations at the interface α/β in the matrix α and the precipitate β, respectively.

Solute is removed from the matrix as the precipitate grows but since the temperature is fixed during isothermal growth, the interface compositions must remain fixed at $c^{\alpha\beta}$ and $c^{\beta\alpha}$ if local equilibrium is to be maintained. Note that the concentration $c^{\alpha\beta}$ is affected by the Thomson-Freundlich or the Gibbs-Thomson equation and is in quasi-equilibrium with the surface energy γ and is, strictly speaking, not an equilibrium value. In order to maintain a constant concentration at the interface, the diffusion flux of the solute at the α/β interface must equal the rate at which solute is partitioned from the matrix to the precipitate so that:

$$v(c^{\beta\alpha} - c^{\alpha\beta}) = -D\frac{\partial c}{\partial z}\Big|_{z=z^*} \qquad \text{Equation 3.14}$$

where v is the growth rate, z is a coordinate normal to the interface with the value z^* and D is the solute diffusivity. Note that the concentration gradient is evaluated at the position of the interface, $z = z^*$.

The prominent feature of precipitate growth is that after some incubation time and the formation of a critical nucleus (taken to have a radius, $r = 0$), the precipitate grows by depleting the matrix solute immediately ahead of the advancing interface. At any position z in the matrix phase (i.e. $z > r(t)$) the solute concentration is a monotonically decreasing function of time [107].

3.3.2 Multicomponent Diffusion Growth

In the work done by Robson and Bhadeshia [77], they treated the growth of carbides using a binary approximation, i.e. in terms of the diffusion of the substitutional element alone. This is incorrect because the mass balance equation will not be satisfied for the interstitial solute. For a ternary system like Fe–C–M, where M stands for a substitutional solute, the tie–line will not in general pass through $\bar{c}$ because it is necessary to simultaneously satisfy two conservation equations at the interface, one each for the substitutional element (M = Nb) and carbon, which diffuse at different rates:

$$v(c_M^{\beta\alpha} - c_M^{\alpha\beta}) = -D_M \left.\frac{\partial c_M}{\partial z}\right|_{z = z^*} \qquad \text{Equation 3.15}$$

$$v(c_C^{\beta\alpha} - c_C^{\alpha\beta}) = -D_C \left.\frac{\partial c_C}{\partial z}\right|_{z = z^*} \qquad \text{Equation 3.16}$$

Because $D_C >> D_M$, these equations cannot in general be simultaneously satisfied for the tie–line passing through $\bar{c}$, apparently implying that growth cannot occur with equilibrium at the interface. However, in a ternary alloy there are many tie–lines to choose from at any given temperature because of the extra degree of freedom given by the phase rule. The local equilibrium condition can be maintained by choosing a tie–line which either minimises the concentration gradient of carbon (thus, allowing substitutional solute flux to keep pace) or maximises the gradient of the substitutional solute to compensate for its slower diffusivity. The mass conservation equation can be satisfied simultaneously in two ways. The first is to choose the tie–line which greatly increases the concentration gradient of M to compensate for its lower diffusivity. This would require the carbide to have virtually the same niobium (M) concentration as the matrix with very little partitioning of Nb, but with a sharp concentration spike at the interface in

order to maintain local equilibrium. This is only possible with a very large driving force and hence it is not applicable to niobium carbide precipitation in microalloyed steels [103,100]. The alternative is to select a tie–line which reduces the gradient of carbon to such an extent that the flux of carbon is reduced to a level consistent with that of niobium.

The intersection of the vertical line with the α / (α + β) phase field defines the tie–line completely which fixes the interface compositions in a manner which satisfies the conservation conditions because the large diffusion coefficient of carbon is compensated for by the very small concentration gradient of carbon. All this assumes that the far field concentration $\bar{c}$ does not change during transformation, i.e. there is no 'soft–impingement' of the diffusion of different particles and very short annealing times that prevail. Note that this also maintains local equilibrium at the interface since the compositions at the interface (given by the points **c** and **d** for α and β respectively) are connected by a tie–line on the phase diagram. The locus of the matrix composition due to solute depletion during precipitation is along the direction **b** $\rightarrow$ **e** (Figure 3.8). The change in the matrix composition leads to a different choice of tie–line, the locus of $c^{\alpha\beta}$ being along **c** $\rightarrow$ **f**. This tie–line shifting continues until the reaction stops when the tie–line intersects the average composition **a** and $c^{\alpha\beta}$ = **f**.

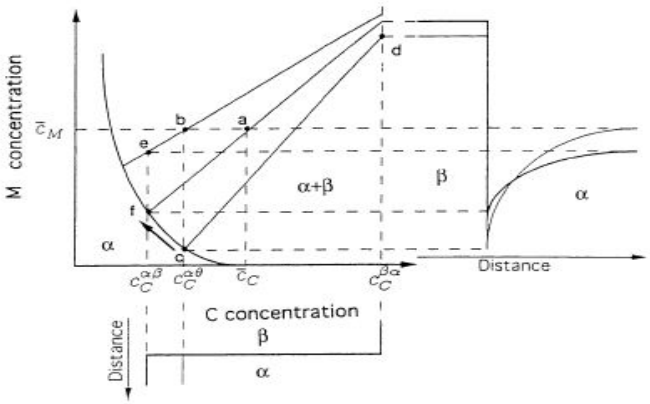

Figure 3.8. A schematic isothermal section through the Fe-C-M phase diagram, showing the ferrite matrix α and alloy carbide β fields. The alloy composition is plotted as point a [4].

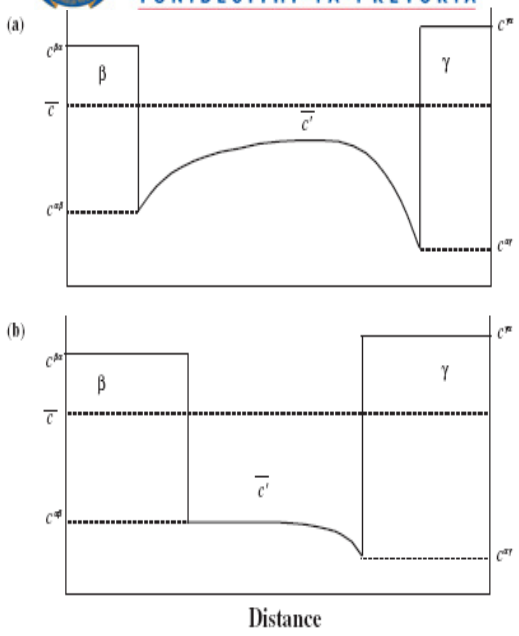

Figure 3.9. Distribution of the solute when (a) both (β) and (γ) are precipitating, and (b) where the precipitation of (β) has been completed. Note that $\overline{c'}$ is the instantaneous solute concentration in the matrix (α) [99].

The mean field approximation can be used to calculate the change in $\overline{c}$ as precipitation proceeds. The instantaneous value of the matrix composition $\overline{c'}$, is given by:

$$\overline{c'} = \overline{c} - \frac{V^{\beta}(c^{\beta\alpha} - \overline{c})}{1 - V^{\beta}} \qquad \text{Equation 3.17}$$

Once the interface compositions are defined as described previously, established theory for diffusion-controlled growth can be applied to estimate the particle radius r as a function of time:

$$r = \alpha_3 \sqrt{D_M t} \text{ with } \alpha_3 \approx \sqrt{2\frac{\overline{c} - c^{\alpha\beta}}{c^{\beta\alpha} - \overline{c}}} \qquad \text{Equation 3.18}$$

where α_3 is the three-dimensional parabolic rate constant and this equation can only be used in the absence of the knowledge of interfacial energy or the shape of the nucleus.

The driving force for nucleation must also be affected by the soft impingement. To deal with this, the extent of the reaction parameter Φ is defined as follows:

$$\Phi = \frac{V^{\beta}}{V^{\beta\alpha}} \text{ with } V^{\beta\alpha} = \frac{\overline{c} - c^{\alpha\beta}}{c^{\beta\alpha} - c^{\alpha\beta}} \qquad \text{Equation 3.19}$$

where V^{β} is the instantaneous fraction, and $V^{\beta\alpha}$ is the maximum fraction of a given phase. The function Φ ranges from 0 to 1 and represents the fraction of excess solute remaining in the matrix relative to the equilibrium composition of the precipitate. It is assumed that the driving force (ΔG_v in Equation 3.9) for the precipitation is linearly related to Φ:

$$\Delta G_v = (1-\Phi)\Delta G_{vo} \qquad \text{Equation 3.20}$$

where ΔG_v and ΔG_{vo} are the driving forces for precipitation at an arbitrary instant and at t=0, respectively.

3.4 TRANSFORMATION KINETICS

The evolution of volume fraction of the second phase during transformation can be described using the well known *Johnson-Mehl-Avrami-Kolmogorov* (*JMAK*) equation [95], which, for spherical particles and isothermal conditions, can be expressed as

$$V_v = 1-\exp\left(-\frac{1}{3}\pi\dot{N}G_r^3 t^4\right) \qquad \text{Equation 3.21}$$

where $\dot{N}$ is the nucleation rate, G_r is the growth rate and t is time. Equation 3.17 above is for the special case of homogeneous nucleation. However, most nucleation in steels occurs heterogeneously, for instance, with the possibility of nucleation on a grain boundary that may be higher than that on other nucleation sites. There are three types of nucleation sites on grain boundaries for the nucleation to take place: planes, edges and corners [100]. In practice, the volume fraction V_v of the second phase is determined as a function of time and this produces a very frequently found sigmoidal or S-shaped curve. A more general form of the *JMAK* equation usually used in practice, takes the form of:

$$V_v = 1-\exp\left(-kt^n\right) \qquad \text{Equation 3.22}$$

where k is a rate constant, subsuming effects associated with nucleation and growth, and is usually empirically evaluated for each temperature, n is the time exponent, often called the Avrami exponent. For this equation to be valid, a plot of $\{\ln\ln [1/(1-V_v)]\}$ vs $\{\ln t\}$ should be linear with a slope n and intercept $\ln k$. Table 5 shows the theoretical values of n and k.

Table 5. Values of *n* and *k* in the general form of Equation 3.19, S_{gb} is the area of grain boundary per unit volume, L_{gb} is the length of grain boundary edges per unit volume and N_c is the density of grain boundary corners. All nucleation on the grain boundaries is assumed to occur before growth [108].

Nucleation site	Time exponent, *n*	*k* – value
Homogeneous nucleation	4	$\frac{\pi}{3}\dot{N}G_r^3$
A plane on grain boundary	1	$2S_{gb}L_{gb}$
An edge on the grain boundary	2	$\pi L_{gb}G_r^2$
A corner on grain boundary	3	$\frac{4}{3}\pi N_c G_r^3$

3.5 Overall Transformation Kinetics

The Johnson-Mehl-Avrami-Kolmogorov (*JMAK*) approach treats the precipitation kinetic problem as an overall kinetic theory. Robson and Bhadeshia developed a simultaneous precipitation reaction model by extending the classical *JMAK* concept of extended space to many phases [109]. Fujita and Bhadeshia improved that model to deal with carbide size and to account for the capillarity effect [100]. In their work, the *JMAK* theory has been applied to describe the kinetics of the single phase in a power plant steel, utilising MTDATA software to predict the driving forces.

3.5.1 The Robson and Bhadeshia Model

In a simple simultaneous reaction in which both β and θ precipitate at the same time from the parent α-phase, it is assumed that the nucleation and growth rate do not change with time and that the particles grow isotropically. If only β is formed, the untransformed α will contribute to the real volume of β. On average, a fraction

$[1 - (V_\beta + V_\theta)/V]$ of the extended volume will be in the previously untransformed material. It follows that the increase in real volume of β is given by the change in extended volume dV_β^e:

$$dV_\beta = \left(1 - \frac{V_\beta + V_\theta}{V}\right) dV_\beta^e \qquad \text{Equation 3.23}$$

and, similarly for θ

$$dV_\theta = \left(1 - \frac{V_\beta + V_\theta}{V}\right) dV_\theta^e \qquad \text{Equation 3.24}$$

In general, V_β is a complicated function of V_θ and it is not possible to analytically integrate these equations to find the relationship between the actual and extended volumes. However, in certain simple cases, it is possible to relate V_β to V_θ by multiplication with a suitable constant K:

$$V_\theta = KV_\beta \qquad \text{Equation 3.25}$$

Equations 3.20 and 3.21 can then be rewritten as:

$$dV_\beta = \left(1 - \frac{V_\beta + KV_\beta}{V}\right) dV_\beta^e \qquad \text{Equation 3.26}$$

$$dV_\beta = \left(1 - \frac{V_\theta + KV_\theta}{KV}\right) dV_\theta^e \qquad \text{Equation 3.27}$$

Accordingly, the final expressions of the volume fractions of β and θ phases are:

$$V_\beta = \left(\frac{1}{1+K}\right)\left\{1 - \exp\left[-\frac{1}{3}(1+K)\pi \dot{N}_\beta G_{r,\beta}^3 t^4\right]\right\} \qquad \text{Equation 3.28}$$

$$V_\theta = \left(\frac{K}{1+K}\right)\left\{1 - \exp\left[-\frac{1}{3}\left(\frac{1+K}{K}\right)\pi \dot{N}_\theta G_{r,\theta}^3 t^4\right]\right\} \qquad \text{Equation 3.29}$$

In practice, the multiple reactions found in most industrial steels have important complications not included in the model above. Precipitation reactions may affect each other by removing solute atoms from the matrix. Any change in the matrix composition must alter the nucleation and growth rates of the phases. Therefore, there are no simple constants linking the volume fraction of all the phases and a different approach is needed.

3.5.2 Fujita And Bhadeshia Model

The Robson and Bhadeshia model can be used to estimate the volume fraction of carbides but it would be useful also to treat particle sizes and coarsening after growth. This has been achieved by Fujita and Bhadeshia, who attempted to take better account of multicomponent diffusion and capillarity [100]. Given the small equilibrium volume fraction of carbides in most ferritic steels, they also relaxed the extended volume concept to permit particle sizes to be calculated approximately.

3.6 CAPILLARITY

The state of equilibrium between two phases changes with the curvature of the interface separating them. This is the well established Gibbs–Thompson capillary effect and is due to the curvature of the interface that then influences the change in equilibrium compositions at the particle/matrix boundary. The free energy change of the particle phase varies relatively sharply with a deviation from the stoichiometric composition so it can be assumed that the particle composition is insensitive to the curvature. However, the equilibrium composition of the matrix changes as follows [99,101,103,104,110]:

$$c_r^{\alpha\beta} = \left(1 + \frac{\gamma}{kT}\frac{\upsilon^{\beta}}{r}\frac{1 - c^{\alpha\beta}}{c^{\beta\alpha} - c^{\alpha\beta}}\right)c^{\alpha\beta} \qquad \text{Equation 3.30}$$

where $c_r^{\alpha\beta}$ is the solute concentration in the α matrix that is in equilibrium with a spherical particle of β and r is the radius of curvature, which in this case also defines the instantaneous particle size. The term $c^{\alpha\beta} = c_r^{\alpha\beta}$ when $r = \infty$. The modified composition $c_r^{\alpha\beta}$ is, therefore, relatively easy to estimate for each particle. At some critical value where $r = r_c$ (where r_c is a critical radius) and $c_r^{\alpha\beta} = \bar{c}$, growth ceases and coarsening starts.

Note in particular in the case of the determination of the particle density measurements, that the number of particles per unit volume N_v first increases, as would be expected during the nucleation stage, but that soon thereafter it starts to decrease, as would be expected for the coarsening stage. This transition generally takes place after only a few minutes of annealing [111].

For a ternary alloy, capillarity is approximated by calculating the $\alpha / (\alpha + \beta)$ phase boundary on an isothermal section of the phase diagram, as a function of r, using Equation 3.30. Equation 3.30 is used to calculate $c_{r,C}^{\alpha\beta}$ and $c_{r,M}^{\alpha\beta}$ for a fixed value of interface radius of curvature r. The growth velocity can then be calculated using the curvature-modified phase boundary. Embryo particles that are smaller than the size of the critical nucleus obviously cannot grow and will dissolve again. Nucleation occurs statistically by random fluctuations in composition so that the growth part in the

computational scheme must start beyond the nucleation stage. Particles nucleate at different times during the course of the reaction, giving rise to a distribution of sizes.

At any given stage of precipitation, the smaller particles will grow at a slower rate than a larger particle because the capillary effect reduces the supersaturation at the interface for small particles. Capillarity has the consequence that large particles have lower solute concentrations at the interface $c_r^{\alpha\beta}$ than small particles [112]. This drives coarsening, which becomes a natural consequence of the precipitation theory, since changes including the dissolution of particles, continue to happen as long as there are solute concentration gradients.

3.7 Dissolution of the Metastable Phase

With soft-impingement being considered, the mean solute concentration within the matrix alone decreases as the reaction proceeds. Each precipitating phase will consume or reject atomic species into the untransformed matrix, whose subsequent transformation behaviour will be altered. Consider the precipitation of β and γ from an α ferrite matrix, which initially has a uniform composition. Schematic composition profiles are shown in the earlier Figure 3.9 (a) of how the distribution of the solute might change during precipitation at the intermediate stage when both the metastable β phase and the equilibrium γ phase are precipitating in the matrix of α simultaneously. Also from Figure 3.9 (b) when the solute concentration in the matrix reaches equilibrium with β; precipitation of β has been completed and as γ precipitates further removing solute, β will start to dissolve. For the situation illustrated, the maximum fraction $V^{\beta\alpha}$, of each phase is given by a lever rule (see Equation 3.19).

3.8 Particle Coarsening

3.8.1 Diffusion Controlled Coarsening of the Particles within Matrix

The coarsening of particles occurs (even though the transformation is said to be completed) when there is no significant change in the precipitate volume fraction over a period of time. Note that it is traditional to separate transformation growth and coarsening but the two processes are in fact both fulfilled with capillarity effects. The coarsening rate of precipitates can be calculated using the classical theory of the Ostwald ripening equation that is due to Lifshitz and Slyozov [113] and Wagner [114]

and is often called *LSW* coarsening. The *LSW* coarsening rate equation for diffusion controlled coarsening is given by:

$$r^n - r_o^n = \frac{8\gamma \upsilon^\beta D c^{\alpha\beta}}{9RT} t \qquad \text{Equation 3.31}$$

where r is the average particle radius, r_0 the initial average particle radius (a fictitious value as no particles exist at t = 0), γ is the interfacial energy, D is the diffusion coefficient of the rate controlling species, υ^β is the molar volume of the phase β, $c^{\alpha\beta}$ is the equilibrium solute concentration in the α matrix at which $r \to \infty$, R is the gas constant, T is the absolute temperature, t is the holding time at the isothermal heat treatment temperature. For intragranular particles it can be assumed that the coarsening of the particles is controlled by bulk diffusion, therefore n =3.

3.8.2 Diffusion Controlled Coarsening of the Particles on Grain Boundary

The above Equation 3.31 is only valid for diffusion controlled coarsening of the particles within the matrix. But there are some scenarios whereby the particles in the grain boundaries coarsen through the diffusion of the solute atoms down the grain boundary. Here, there is a two dimensional diffusion down the grain boundary from the smaller particle to the larger particle. The theory is basically the same as for matrix diffusion and the coarsening rate equation changes to:

$$r^4 - r_o^4 = \frac{K_1 \gamma \upsilon^\beta D_{gb} c^{\alpha\beta} \delta_{gb}}{kT} t \qquad \text{Equation 3.32}$$

where K_1 is a constant, D_{gb} = diffusion coefficient down the grain boundary, δ_{gb} = width of the grain boundary and t = time at temperature. The above coarsening Equation 3.32 is also only fully valid if all of the precipitates were situated on grain boundaries and this, of course, is quite difficult to achieve. It may be approximated, however, by introducing a subgrain structure into the matrix in which, very often, most of the particles are “captured” by the subgrain boundaries. In the work by Kostka et al.[115] and Mukherjee et al.[116], the authors observed that the grain boundary carbides coarsen faster than the matrix carbides.

3.8.3 DIFFUSION CONTROLLED COARSENING OF THE PARTICLES ON SUBGRAIN BOUNDARIES

This mechanism may be found in cases where high temperature creep at a service temperature takes place and all of the precipitates become entangled and are, in fact, interconnected by dislocations in subgrain boundaries:

$$r^5 - r_o^5 = \frac{K_1 \gamma \upsilon^\beta D_{disl} c^{\alpha\beta} \delta_{disl} N'}{kT} t \qquad \text{Equation 3.33}$$

where K_1 = constant, δ_{disl} = effective diameter of a dislocation, N' = number of dislocations that meet each particle and D_{disl} = diffusion coefficient down a dislocation. Direct experimental evidence of this power law has not been obtained although many cases of direct and indirect evidence do exist that precipitates that are situated on subgrain boundaries, grow at a faster rate than others.

3.9 SUMMARY

Many researchers have modelled and calculated the values for the interfacial energy of the M_6C carbide and Laves phase in Fe–C–Nb systems and have estimated them to be 0.286 Jm^{-2} [103] and 0.331 Jm^{-2} [77,117,118], respectively. From these results, because of a complex unit structure of the Laves phase, its interfacial energy seems to be larger than that of M_6C carbide as would be expected. In other work also done on the Fe–C–Nb systems by Sim et al. [3], they have assumed a much higher value of 1.0 Jm^{-2} for the Fe_2Nb Laves phase because of its incoherency with the α-matrix.

Fujita et al., [99] using the *MTDATA* thermodynamic software, have modelled the precipitation kinetics in the Fe-Nb-C system for a 9Cr-0.8Nb steel at 950°C. The precipitation sequence was found to be as follows:

$$\alpha \rightarrow \alpha + Nb(C,N) + Fe_2Nb + Fe_3Nb_3C \rightarrow \alpha + NbN + Fe_3Nb_3C$$

and this shows that in this steel the equilibrium phases are NbN and Fe_3Nb_3C, and the Laves phase is a meta-stable phase. Figure 3.10 shows the comparison between the experimental and the calculated phases in obtaining the precipitation sequencing.

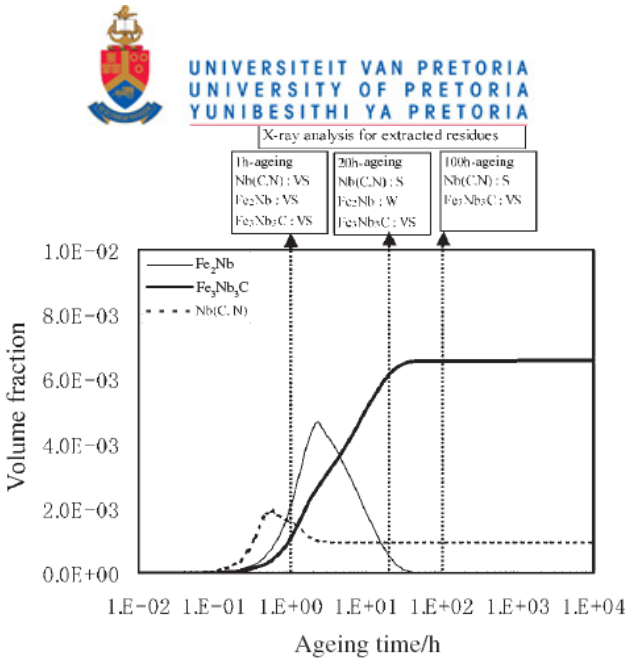

Figure 3.10. The kinetics of the precipitation sequence in 9Cr-0.8Nb ferritic stainless steel [101].

CHAPTER FOUR

EXPERIMENTAL PROCEDURES

4.1 MATERIALS

Type 441 ferritic stainless steel which is a niobium and titanium dual stabilised steel, was studied in this work. The main emphasis was on understanding the formation of the intermetallic Laves phase and its impact on the toughness of this steel. Steels A and B were supplied from Columbus Stainless in the hot rolled condition with Steel A having not received any water cooling on the hot mill's run out table due to a system failure. This coil was found to be too brittle to be processed further and was, therefore, made available for this study while specimens of Steel B were as processed normally with adequate laminar flow cooling after hot rolling.

The effect of the alloy's chemical composition was also investigated through two experimental alloys that were within the type 441 ferritic stainless steel's specification. The first experimental alloy identified as Steel C, i.e. a Nb–Ti alloy, is similar to Steel A but has a higher carbon content (almost double that of Steel A's 0.012%C) and lower Nb content of only 0.36%Nb if compared to the Steel A's Nb-content of 0.44%. The second experimental alloy identified as Steel D, is a Nb–Ti–Mo alloy very similar to Steel A but contains an additional ~0.5 wt.% Mo. The effect of even higher molybdenum (Mo) additions was studied on AISI type 444 ferritic stainless steel, that is Steel E, which is a high Mo containing steel with the nominal composition of 18Cr–2Mo; this alloy is also a dual stabilised ferritic steel with a slightly lower content of niobium and titanium. Table 4.1 shows the chemical compositions of the alloys used in the present study while Figure 4.1 shows the detailed flow chart of the research plan to study the nucleation and kinetic models for the Laves phase precipitation and its effects on the impact toughness of the AISI type 441 stainless steel.

Table 4.1. Chemical composition (in %wt) of ferritic stainless steel studied in this work.

Elements	Supplied by Columbus		Hot rolled experimental alloys		
	Steel A 441 SS[†]	Steel B 441 SS[‡]	Steel C Nb-Ti	Steel D Nb-Ti-Mo	Steel E 444 SS[§]
C	0.012	0.015	0.023	0.012	0.014
Mn	0.51	0.54	0.46	0.35	0.45
Co	0.03	0.02			0.02
Cr	17.89	17.9	17.9	17.6	18.3
B	0.0004	0.0006			0.0006
V	0.12	0.14			0.12
S	0.001	0.002	0.0073	0.0018	0.003
Si	0.5		0.33	0.31	0.47
Ti	0.153	0.149	0.171	0.171	0.106
Ni	0.19	0.19	0.13	0.12	0.15
N	0.0085	0.021	0.024	0.026	0.016
Al	0.009	0.009	0.011	0.013	0.01
P	0.025	0.023	0.024	0.032	0.024
Cu	0.08	0.09	0.07	0.06	0.12
Nb	0.444	0.445	0.36	0.39	0.251
O	0.0076				
Mo		0.008	< 0.01	0.54	1.942

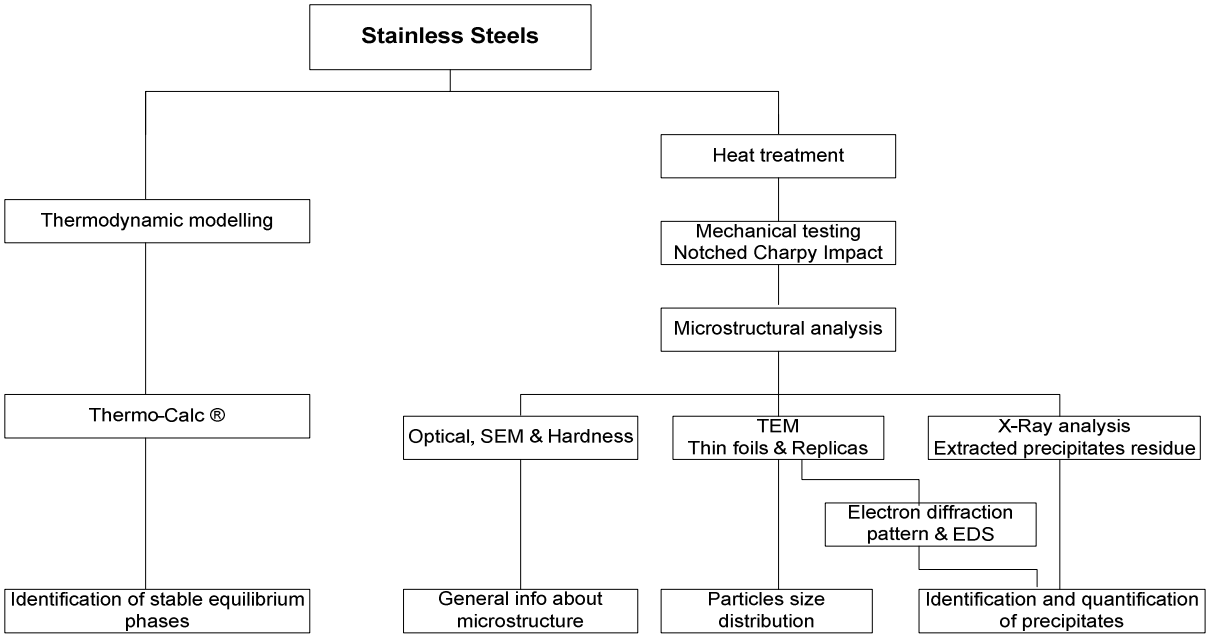

Figure 4.1. Experimental plan.

[†] Columbus Stainless MPO Number 3533603- failed during production
[‡] Columbus Stainless MPO Number 3658671 – didn't fail
[§] Columbus Stainless MPO Number 3631171

4.2 THERMODYNAMIC MODELLING

Modelling precipitation in AISI type 441 ferritic stainless steel requires knowledge of both thermodynamic and kinetic parameters for a variety of possible phases. To obtain these parameters, the computer package Thermo-Calc® version Q (TCFE3 database [119]) thermodynamic software was used to make these thermodynamic calculations. All of these experimental alloys were initially modelled to determine the precipitation temperatures of the phases present, in particular the Laves phase. This has assisted in designing a suitable heat treatment for this alloy without causing major grain growth. A detailed modelling procedure is given in Chapter 5.

4.3 HEAT TREATMENTS

The results obtained from the Thermo-Calc® modelling were used as guidance for designing an appropriate heat treatment for the alloys. The effect of the Laves phase embrittlement was studied by subjecting the specimens to different heat treatments in an inert argon atmosphere.

4.3.1 LAVES PHASE DISSOLUTION/PRECIPITATION TEMPERATURES

The first step was to determine the annealing temperatures at which the Laves phase dissolves and its impact on the mechanical properties of the steel during its re-precipitation. Most of the annealing treatments were designed around the solvus temperature of the Laves phase, which is within the range of 780 to 950 °C depending on the composition of the alloy, as reported in the literature and calculated by Thermo-Calc® predictions. Steel A was used for this part of the study and the specimens were annealed within the temperature range of 600 to 1100 °C for 30 min. followed by water quenching.

4.3.2 HEAT TREATMENT FOR THE EMBRITTLING EFFECT

Heat treatments for embrittlement of the specimens from AISI type 441: Steel A were performed on:

(1) Charpy impact specimens that had first been solution annealed at 950 °C for 1hr to dissolve the Laves phase and then quenched in water. These specimens were then reheated within the temperature range of 600 to 900°C for 30 min to re-precipitate the Laves phase and were then water quenched, see Figure 4.2. From these specimens the effect of the Laves phase re-

precipitation at different temperatures on the upper – shelf energy and DBTT in Steel A could be studied.

(2) A second set of experiments was used to determine the effect of cooling rate from typical hot rolling temperatures on the embrittlement of these materials through the application of programmed linear cooling rates on the specimens from the solution treating temperature. The programmed cooling rates were applied to specimens in a Gleeble® 1500D Thermal Simulator using subsize Charpy specimens that were annealed at 850 and 950 °C respectively for 5 minutes in an inert argon atmosphere followed directly by forced cooling with helium at different linear cooling rates ranging from 1 to 60 °C/sec, see Figure 4.3.

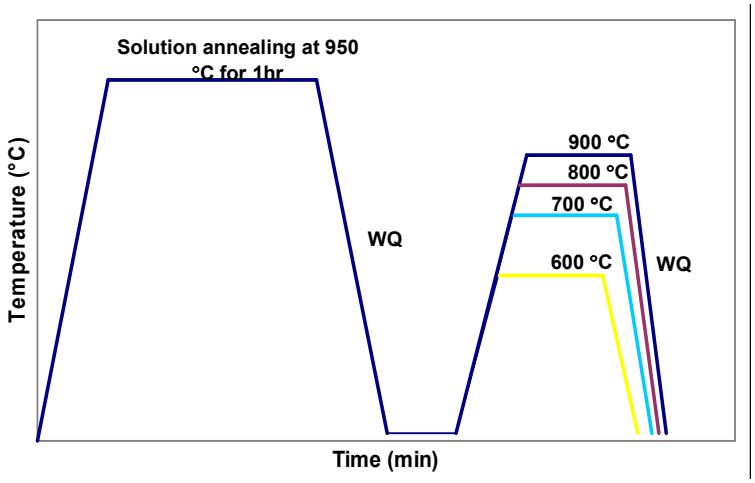

Figure 4.2. Embrittlement through reheating to determine the effect of the Laves phase re-precipitation on the DBTT and upper shelf energy of steel A.

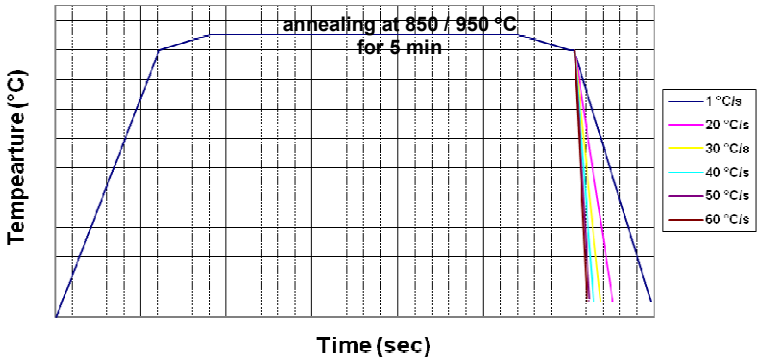

Figure 4.3. Embrittlement through cooling to determine the effect of the Laves phase re-precipitation on the Charpy impact toughness.

4.3.3 HOT-ROLLING OF EXPERIMENTAL ALLOYS

The experimental alloys C and D were prepared by Mintek in a 5 kg vacuum induction melting furnace (VIM) using scrap from Steel A as base scrap material. The as-cast alloys were homogenised in an argon atmosphere at 1200 °C and hot forged to bars of about 30 mm thick. Steel E was supplied by Columbus Stainless as a 28 mm thick hot-band material. Subsequently, these three steels, i.e. C, D and E were solution treated at 1200 °C for 1hr followed by hot rolling to a final thickness gauge of 5.5 to 6.0 mm and quenched in water. The average last pass temperature before quenching was approximately 950°C, which is above the calculated Laves phase formation temperature.

4.3.4 LAVES PHASE KINETIC STUDY

The study of the Laves phase kinetics was conducted using a small tubular furnace that provided a suitable small temperature gradient, as shown in Figure 4.4. Both the furnace and specimen temperature were monitored and controlled by the data logger model DT500 dataTaker® and PID temperature controller, respectively. A type K thermocouple was spot welded to the specimens to monitor the annealing temperature inside the furnace. Figure 4.5 shows the time- temperature profile of the specimen inside the small tubular furnace. Note that the start of the annealing time was considered from the point whereby the specimen had reached a desired temperature and had stabilised. After annealing for a required period of 1 – 1000 minutes, the specimens were subsequently quenched in water. These specimens where then subjected to the Charpy impact test and also the precipitates were extracted electrolytically from them, see Section 4.6.1.

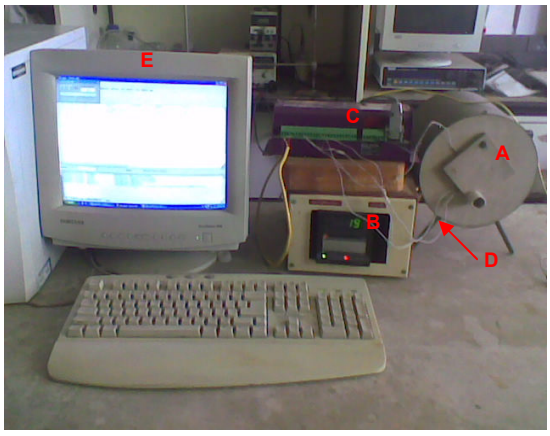

Figure 4.4. The furnace used for the precipitation kinetic study. (A) tube furnace; (B) temperature controller; (d) data logger; (D) type k thermocouple; (E) recording computer.

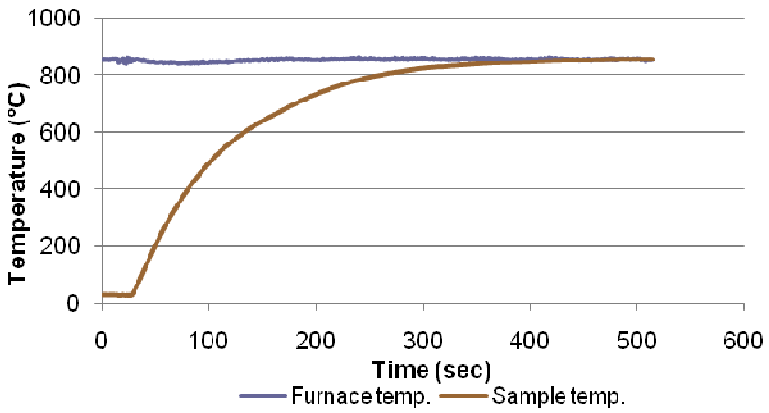

Figure 4.5. The temperature gradient of the Charpy impact specimen inside the furnace.

4.4 MECHANICAL TESTING

4.4.1 TENSILE TESTS

Tensile tests were carried out at a cross head speed of 5 mm/min at room temperature using two subsized specimens prepared according to the ASTM E8[**] standard for each measurement. The longitudinal axes of the specimens were parallel to the rolling direction of the plate throughout. The schematic drawing of the tensile specimen and its dimensions are shown in Figure 4.6 and Table 4.2, respectively.

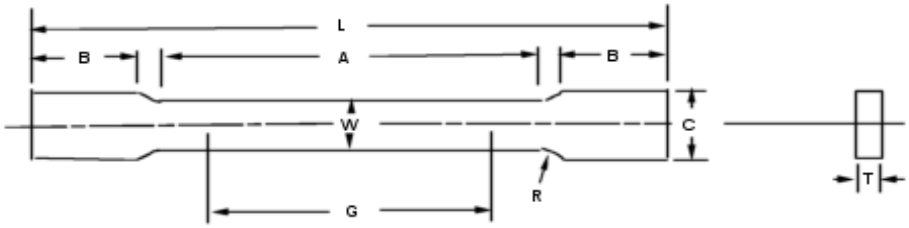

Figure 4.6. Schematic diagram of the subsize tensile test specimen.

Table 4.2. The actual dimensions for the subsize tensile test specimen.

	Parameters	Dimensions (mm)
G	Gauge length	25
W	Width	6
T	Thickness	5
R	Radius of fillet	6
L	Overall length	100
A	Length of a reduced section	32
B	Length of grip section	32
C	Width of grip section	10

[**] ASTM E8 – 08: Standard Test Methods for Tension Testing of Metallic Materials

4.4.2 Notched Charpy Impact Test

Charpy impact test values were obtained as an average from three subsized specimens of 5 x 10x 55 mm^3 prepared according to the ASTM E23[††] standard. A standard 2mm V-notch was made in the specimens after the heat treatment to avoid oxidation effects from the heat treatment at the notch tip. The longitudinal axes of the specimens were parallel to the rolling direction of the plates throughout the study.

The specimens for DBTT Charpy tests were prepared by immersing them in different liquid media to obtain the desired test temperature. For the temperatures higher than 25 °C, heated water controlled by a thermal regulator was used. To achieve a 0 °C testing temperature, icy water was used and below 0 °C, a mixture of dry ice[‡‡] and ethanol or liquid nitrogen[§§] and ethanol were used, depending on the desired lower temperature one wants to reach. The mixtures were prepared inside a thermo flask and different mixing ratios of dry ice to ethanol or liquid nitrogen to ethanol were used to achieve the desired testing temperature. Once the testing temperature was reached the specimens were allowed to settle for about 5 minutes in order to normalise the temperatures before they were subjected to immediate Charpy impact testing.

4.4.3 Hardness Tests

Vickers microhardness measurements were made using a load of 30 kgf to give a relatively large indentation to offset any effects due to localised variation in structure. The average of at least five readings was taken for each result.

4.5 Microanalysis of Specimens

Several types of microscopy were performed to locate, identify, and quantify the microstructural components in the steels after their different treatments, ranging from optical microscopy, scanning electron microscopy to transmission electron microscopy. Analysis of small particles can often prove to be difficult but through a combination of these different techniques coupled with energy dispersive spectroscopy, one can reasonably gain insight into the precipitation behaviour.

[††] ASTM E23 – 02a: Standard Test Methods for Notched Bar Impact Testing of Metallic Materials
[‡‡] Dry ice sublimes at -78.5 °C
[§§] Liquid nitrogen boils at -196 °C

4.5.1 Optical Microscopy

The metallographic specimens were prepared by standard metallographic techniques on a polishing system to a 3μm finish. The specimens were then etched electrolytically in 60% nitric acid in water at a potential of 1.5 V dc for a period of 30 to 120 sec., to optimise the phase contrast and grain size effects. Microstructural analysis was carried out using Olympus PGM and Nikon Eclipse ME600 optical microscopes, both equipped with Analysis™ image software. The grain size was determined using the linear intercept method in accordance to the ASTM E 112 - 96*** standard.

4.5.2 Transmission Electron Microscopy (TEM)

TEM observations were carried out using a Philips CM 200 TEM operating at an accelerating voltage of 160kV and a JOEL JEM – 2100F field emission TEM operating at an accelerating voltage of 200kV.

4.5.2.1 Preparation of TEM Specimens

Two types of specimens were examined using TEM: thin foils and carbon extraction replicas. From these, the types of precipitates were identified using energy dispersive X-ray analysis spectroscopy (EDS) and small angle electron diffraction patterns (SAED).

Thin foils were cut from the bulk materials as 3mm diameter discs of about 1 mm thickness using an electrospark wire cutting device. After cutting, the specimens were attached to a large steel block using hot wax. These specimens were mechanically ground from both sides with silicon carbide paper to less than 70 μm thickness before the wax was dissolved in acetone to release the thinned specimens. Electropolishing was conducted until perforation of the disc occurred using a twin jet electropolisher in a 10 % perchloric acid in 90% acetic acid solution at room temperature at a voltage of 55 dc. Finally, the specimens were cleaned using a four step ethanol cleaning process to remove all residues from the specimens.

Carbon replica specimens were firstly mounted as for metallographic examination and etched the same way. A carbon film was applied by vacuum evaporating carbon onto the etched specimen surface. The carbon film was electrolytically detached in a solution of 5 vol.% hydrochloric acid in methanol at a constant potential of 1.5 V dc after which

*** ASTM E112 – 96: Standard Test Method for Determining Average Grain Size

the replicas were washed using ethanol and then floated off onto distilled water, from where the replicas could be collected on 3 mm diameter copper grids.

4.5.3 Scanning Electron Microscopy (SEM)

The scanning electron microscopy (SEM) investigations were carried out on a Jeol JSM – 6300 and also on a high resolution field emission scanning microscope model Joel JSM – 6000F (SEM). The accelerating voltage was set at 15 kV and the probe current was 7 x 10^{-9} A in both electron microscopes. Both the thin foils and the metallographic specimens were used for the particle's analyses. The advantages of using TEM thin foils in a SEM is that: (1) the specimens are very clean which helps to resolve small particles; and (2) the electropolishing tends to leave fine precipitates on top of the surface, facilitating a good image and analysis of the particles.

4.6 Identification of Precipitates

4.6.1 XRD Study

XRD analysis was carried out on a PANalytical X'Pert Pro powder diffractometer with X'Celerator detector and variable divergence and receiving slits equipped with an Fe-filtered Co-K_α (λ = 1.789 Å) anode as a source of X-rays. The scanning was carried out at an angular range of 20 to 90 (°2 Theta) employing a step size of 0.017° 2 Theta. The generator setting was at 50 mA and 35 kV.

4.6.1.1 Specimen Preparation

X-ray analysis on a larger representative volume of each steel, not only supports the TEM observations from small volumes of materials, but also provides information on the quantity of each phase with a reasonably good accuracy. Electrochemically extracted residues of second phase particles were examined by X-ray powder diffraction to identify the types and volumes of precipitates formed in these alloys. To obtain residues, the precipitates were extracted by means of potentiostatic electrolysis at a constant potential chosen between 100 and 200 mV against a silver chloride electrode in a solution of 10 vol.% acetyl acetone and 1 vol.% tetramethyl ammonium chloride in methanol (TMAC), in which only the iron matrix dissolves [8], leaving a mixture of the second phases behind as a powder residue. Also, the use of 60% nitric acid in water at a potential of 5 V dc to electrolytically extract the particles was found effective in extracting larger volumes of precipitate residue in a short space of time. The residue was vacuum

suction filtered using a sub-micron glass filter paper (≤ 0.7 μm) to trap the fine particles with the filter paper pre-weighed to account for the very fine precipitates that might remain trapped in it during the filtration process. The extracted residues where rinsed with ethanol, dried and weighed to obtain the weight fraction from the previously weighed steel specimen.

4.6.1.2 ANALYSIS

Phase identification was carried out using X'Pert Highscore Plus software, using an integrated interface and fast retrieval software for the *International Centre for Diffraction Data* (ICDD) reference database, flat file format and relational databases. Any number of user reference patterns that have been modified can be added into the reference databases.

Figure 4.7 shows the calculations for user reference patterns for the phases that were expected to be present in these steels. These patterns were generated using the PowderCell 2.4 software and can be read in ICDD structure files by exporting them in a variety of forms into the X'Pert Highscore Plus software. The generation of these patterns requires the knowledge of the symmetry (translational and space group), unit cell data and atomic position parameters, see **Appendix A.**

The complexity in quantification of the carbides and nitrides expected in these steels arises from the structural phases in which these carbides and or nitrides may be formed, i.e. whether the carbides are present as NbC/ TiC and /or NbN / TiN or Nb(C,N) or Ti(C,N) or as (Ti,Nb)(C,N). All of these phases have similar peaks, but the differences arise from the peak's position of each phase, see Figure 4.7. From this figure it can be seen that there is not much of a difference in the peak's position for the carbide and nitride phases of niobium or titanium, but the combination of niobium and titanium, as in (Ti,Nb)(C,N), makes a significant difference in the positions of the peaks.

Note that, in Figure 4.7 and Figure 4.8, both figures show the simulated phase patterns and these are, therefore, not the actual results. PowderCell predictions were based on the assumption of a pure specimen that has equal amounts of phases. Therefore, the results from the precipitate residues will be slightly different from these, and they required a further refinement using Autoquan/BGMN software to obtain an accurate volume fraction for each phase.

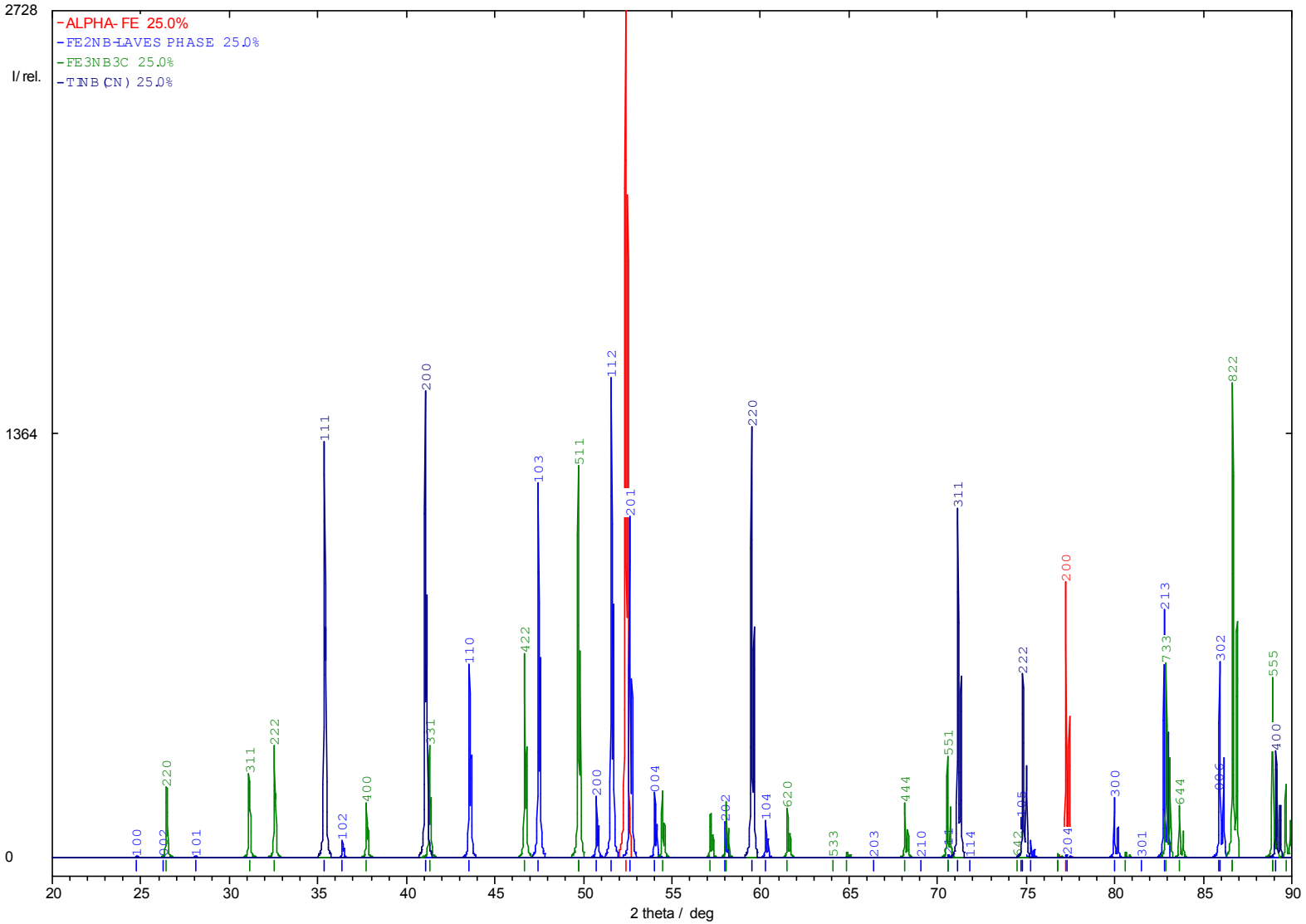

Figure 4.7. The XRD powder pattern of the phases that were expected to be present in type 441 stainless steel as generated using a PowderCell software.

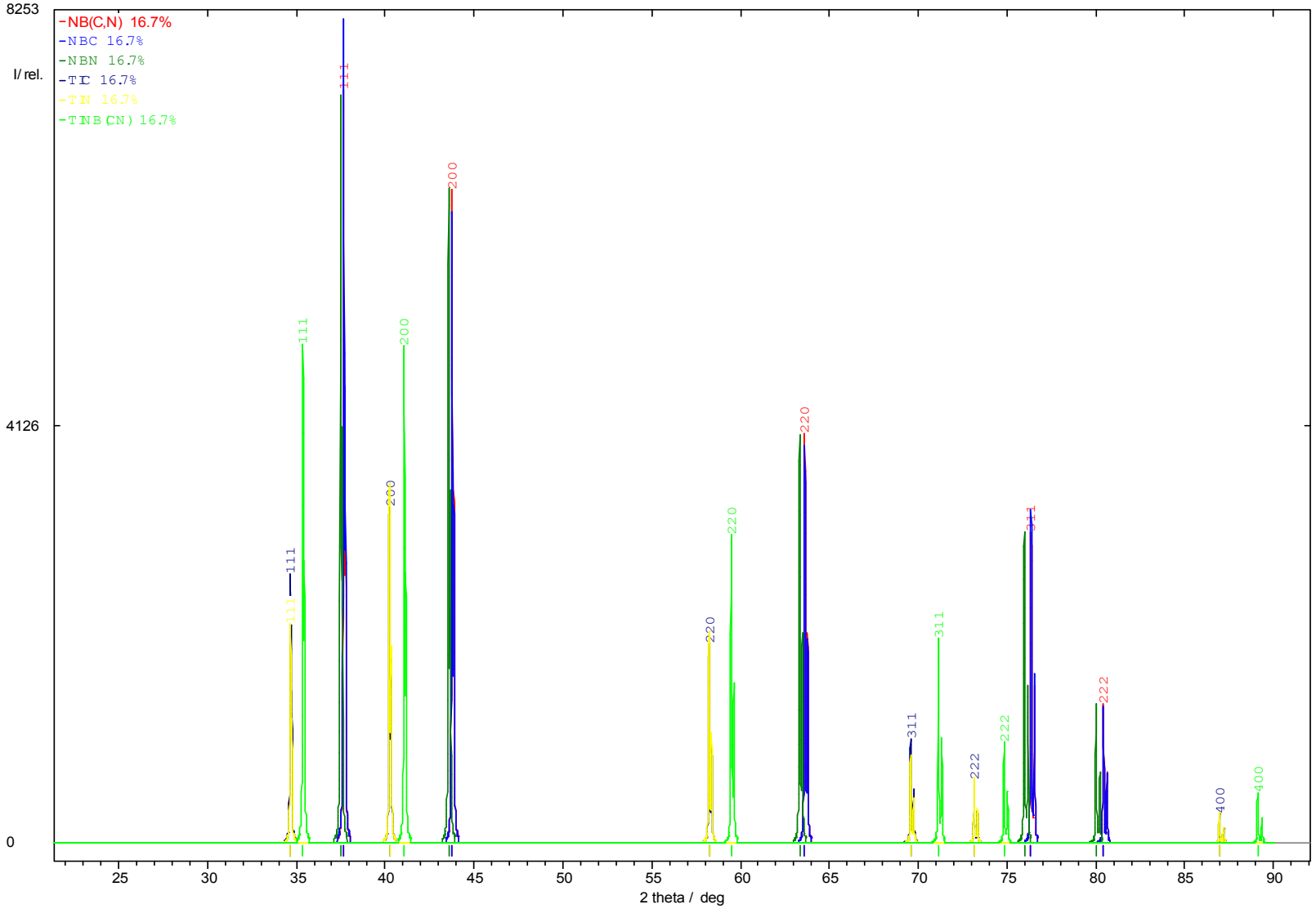

Figure 4.8. The XRD powder pattern showing the peak's positions of the carbide and nitrides of titanium and niobium. Notice the position of the (Ti,Nb)(C,N).

Quantification of the various phases' weight fractions in the powder residue was carried using Autoquan/BGMN software (GE Inspection Technologies) employing a Rietveld refinement approach [120,121]. The quantification was done using the phases' reference data from the ICDD databases or from the user reference database. A typical XRD spectrum from the analysed powder residue after quantification is shown in Figure 4.9. Notice how good is the residual differences (i.e. bottom spectrum) between the calculated and the measured spectrums.

The quantified results from the X-ray analysis are given as weight fraction, therefore for the volume fraction calculation; the densities for each phase are needed. Table 4.3 shows the densities of all phases present in these alloys [122].

Table 4.3. The density of the phase that were used in the quantifications.

Phase	Density (g/cm^3)
Fe_2Nb	8.63
Fe_3Nb_3C	8.44
α-Fe	7.87
Nb,TiC	6.39
NbC	7.80
NbN	8.40
TiC,N	7.82
TiC	4.94
TiN	4.83

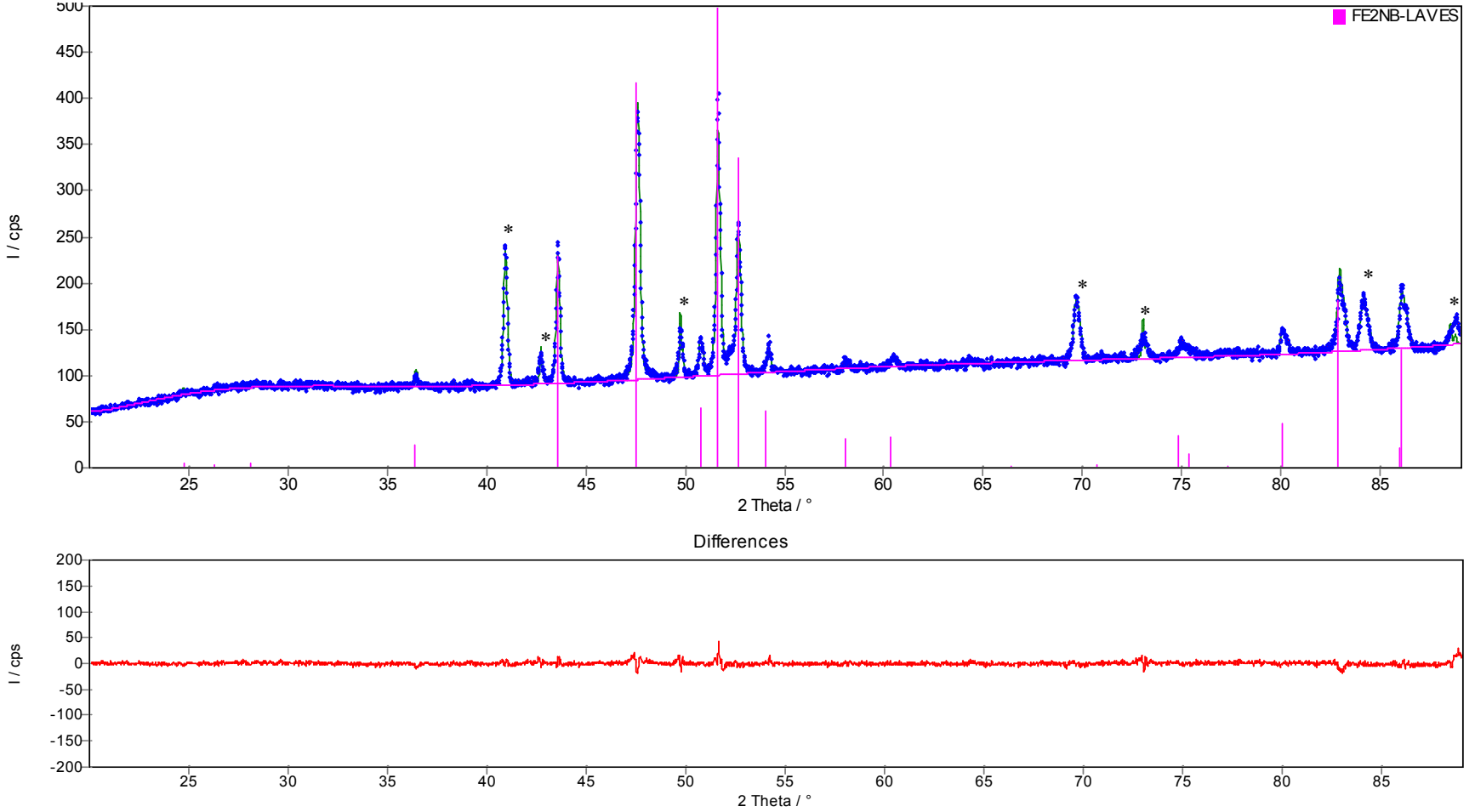

Figure 4.9. A typical XRD scan of the precipitate's residue from Steel A showing the presence of the Laves phase peaks (indicated by the lines in the top figure). The remaining peaks are the carbides and nitrides, indicated by (∗). Note the good residual difference between the calculated and the measured spectrum as is shown by the spectrum below.

4.6.2 ELECTRON DIFFRACTION PATTERNS

Selected area electron diffraction (SAED) patterns of second phases using carbon extraction replicas, is a reliable method to identify unknown precipitates because there is no interference from the matrix. The intended precipitates are chosen using a selected area aperture and a corresponding diffraction pattern is obtained. Figure 4.10 shows the schematic drawing of the geometry of diffraction.

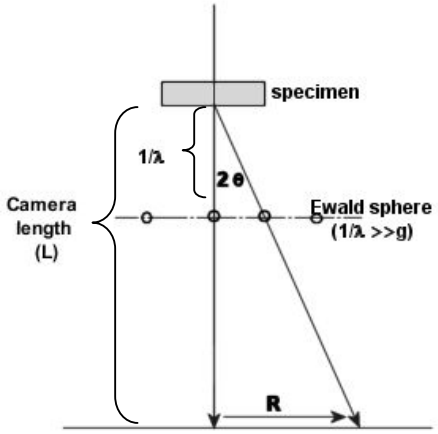

Figure 4.10. The single crystal electron diffraction pattern

R_{hkl} is the distance between the transmitted spot and the diffracted spot from the *hkl* plane. θ_B is the Bragg angle corresponding to the *hkl* plane and L is the camera length. The relationship between these parameters can be described as follows [123,124]:

$$R_{hkl}d_{hkl} = L\lambda \qquad \text{Equation 4.1}$$

where d_{hkl} is the calculated spacing of *hkl* planes and λ is wavelength given by:

$$\lambda = \frac{h}{\sqrt{2meV}}\ \text{Å} \qquad \text{Equation 4.2}$$

$$\lambda = \frac{12.236}{\sqrt{V}}\ \text{Å} \qquad \text{Equation 4.3}$$

Electrons accelerated by a potential difference of V volts have a kinetic energy of $½ mv^2$, where:

$$½ mv^2 = Ve \qquad \text{Equation 4.4}$$

e being the standard for an electron charge.

The wavelength λ is associated with an electron of mass m grams travelling with a velocity ν cm/sec. A relative correction is needed for the actual conditions involving the voltages used, so that the actual formula is slightly more complicated, as follows:

$$\lambda = \frac{12.236}{\sqrt{[V(1+0.9788x10^{-6}V)]}} \text{ Å} \qquad \text{Equation 4.5}$$

The camera constant $(L\lambda)$ was calibrated using a gold film when the electron microscope is operating at 160 kV. From equation 4.5 above, the wavelength (λ) was calculated as 2.84 x 10^{-12} m, and the camera constant $(L\lambda)$ was determined to be 2.70 x 10^{-12} m^2 when using a camera length L of 950 mm.

4.7 The Orientation Relationship Between the Laves Phase and the Matrix

The habit plane and the morphology of the Laves phase precipitates were determined from the thin foil specimens. For simplicity, because of a very small size of the precipitates to be analysed without interference from the matrix, the orientation relationship was determined firstly, by obtaining the pattern from the adjacent matrix followed by the pattern from both the matrix and the precipitates. From the two patterns, one is able to determine the pattern of the precipitate by correlating the two patterns.